



# CHORUS

This is the accepted manuscript made available via CHORUS. The article has been published as:

## Evolution of the surface structures on SrTiO<sub>3</sub>(110) tuned by Ti or Sr concentration

Zhiming Wang, Fang Yang, Zhiqiang Zhang, Yuanyuan Tang, Jiagui Feng, Kehui Wu, Qinlin Guo, and Jiandong Guo

Phys. Rev. B **83**, 155453 — Published 28 April 2011

DOI: [10.1103/PhysRevB.83.155453](https://doi.org/10.1103/PhysRevB.83.155453)

# Evolution of the Surface Structures on SrTiO<sub>3</sub>(110) Tuned by Ti or Sr Concentration

Zhiming Wang, Fang Yang, Zhiqiang Zhang, Yuanyuan Tang, Jiagui Feng, Kehui Wu, Qinlin Guo, and Jiandong Guo\*  
*Beijing National Laboratory for Condensed-Matter Physics & Institute of Physics,  
 Chinese Academy of Sciences, Beijing 100190, P. R. China*  
 (Dated: February 22, 2011)

The surface structure of the SrTiO<sub>3</sub>(110) polar surface is studied by scanning tunneling microscopy and X-ray photoelectron spectroscopy. Monophased reconstructions in (5×1), (4×1), (2×8), and (6×8) are obtained, respectively, and the evolution between these phases can be tuned reversibly by adjusting the Ar<sup>+</sup> sputtering dose or the amount of Sr/Ti evaporation. Upon annealing, the surface reaches the thermodynamic equilibrium that is determined by the metal concentration. The different electronic structures and absorption behaviors of the surface with different reconstructions are investigated.

PACS numbers: 68.47.Gh, 68.37.Ef, 68.35.Md, 82.80.Pv, 68.35.Rh

## I. INTRODUCTION

Perovskite oxides possess a wide variety of valuable properties such as superconductivity, colossal magnetoresistance and photocatalytic reactivity that are of interest for numerous technological applications. Knowing the detailed structure of oxide surfaces is extremely important to understand the underlying physics and chemistry. During the past decade, a tremendous amount of evidence has shown that oxide thin films, superlattices and heterostructures display an even richer diversity of remarkable properties<sup>1</sup>. One of the important and intriguing discoveries is the quasi-two-dimensional electron gas (2DEG) formed at the interface between SrTiO<sub>3</sub> and LaAlO<sub>3</sub><sup>2</sup>, which might be the basis of the transformative concept for the new generation of electronic devices<sup>3</sup>. Additionally, Hwang *et al.* found that the formation of 2DEG critically depends on the atomic arrangement at the interface – it can be formed only if the SrTiO<sub>3</sub> substrate is terminated by the TiO<sub>2</sub> layer, while the interface is insulating when the substrate exposes the SrO layer<sup>2</sup>. Therefore it is indispensable to control the surface structure of perovskite oxides as well as the epitaxial growth with atomic precision.

Single crystalline SrTiO<sub>3</sub> is widely used as the epitaxial growth substrate for complex perovskite oxide films and heterostructures<sup>2,4-9</sup>. By selective chemical etching of the SrO layer followed by thermal annealing, atomically well-defined SrTiO<sub>3</sub>(001) surface can be achieved<sup>10,11</sup>. Microscopic studies have shown a series of reconstructions. Either Sr<sup>12,13</sup> or Ti<sup>14-17</sup> rich phase has been observed on the surface depending on preparation methods. The Sr adatom model consisting of ordered Sr adatoms on a TiO<sub>2</sub> terminated layer has been proposed for the ( $\sqrt{5} \times \sqrt{5}$ )-R26.6° reconstruction based on first-principles total-energy calculations<sup>12</sup>. Transmission electron microscopy (TEM)<sup>14,15</sup> and surface x-ray diffraction<sup>18</sup> studies showed a double-layered TiO<sub>2</sub> structure formed on the (2×1)- and c(4×2)-reconstructed surfaces, respectively. It has been revealed that the stability of the surface phases strongly correlates to the stoichiometry<sup>19-22</sup>.

Along (110) direction, SrTiO<sub>3</sub> single crystal is com-

posed of alternately stacked (SrTiO)<sup>4+</sup> and (O<sub>2</sub>)<sup>4-</sup> atomic layers (see Fig. 1), which creates a macroscopic dipole perpendicular to the surface<sup>23,24</sup>. Therefore the surface is inherently unstable. On one hand, this means that manipulating the polarity provides us an additional degree of freedom to tune the properties of the oxide multilayers<sup>25</sup>. On the other hand, in order to cancel the surface polarity and thus making the electrostatic energy converged, a polar surface bears high reconstruction instability<sup>24</sup>. Besides several (1×1) terminations proposed by the *ab initio* calculations<sup>26</sup>, a large family of reconstruction has been observed on SrTiO<sub>3</sub>(110) surface. Brunen and Zegenhagen<sup>27</sup> observed (2×5), (3×4), (4×4), (4×7), and (6×4) reconstructions by scanning tunneling microscopy (STM), low energy electron diffraction (LEED), and Auger electron spectroscopy (AES) measurements and found that the surface Sr concentration increases with elevated annealing temperatures. Bando *et al.*<sup>28</sup> obtained (5×2) and c(2×6) reconstructed surfaces exhibiting metallic characteristics. Recently, M. R. Castell *et al.*<sup>29</sup> observed an (n×1) (3≤n≤6) family of reconstruction. Their AES analyses revealed that the (3×1) and (4×1) were Ti-enriched, while the (6×1) was Sr-enriched. Combined with TEM and density functional theory studies, they proposed a corner-sharing TiO<sub>4</sub> tetrahedra model<sup>30</sup>.

Our previous studies showed that thermodynamically stable SrTiO and O-terminations can be obtained on SrTiO<sub>3</sub>(110) surface by Ar<sup>+</sup> sputtering followed by annealing in ultra high vacuum (UHV)<sup>31</sup>. In this paper we establish the phase diagram of SrTiO<sub>3</sub>(110) surface in a wide scale, covering from the (5×1)- to (4×1)-reconstructed surface of SrTiO termination, then to (2×8)- and finally to (6×8)-reconstructed surface of O termination. The concentration ratio of near surface region metal cations, [Ti]/[Sr], increases when the reconstruction evolves between the above phases sequentially as determined by the X-ray photoelectron spectroscopy (XPS) analyses. We find that the reconstruction phases can be selected by adjusting [Ti]/[Sr], which can be tuned by two methods equivalently - to adjust the evaporation dosage of Ti or Sr onto the surface, or to adjust the Ar<sup>+</sup>

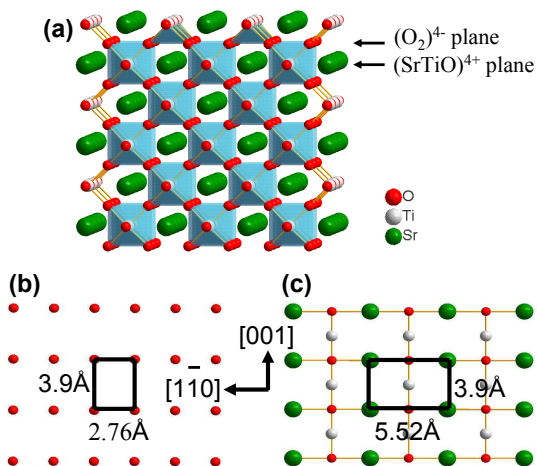


FIG. 1: (Color online) (a) Ball model of the  $\text{SrTiO}_3(110)$  surface. The interspacing of adjacent  $(\text{O}_2)^{4-}$  and  $(\text{SrTiO})^{4+}$  planes is  $1.38 \text{ \AA}$ . (b) and (c) The corresponding top view of O and SrTiO planes, respectively. The irreducible unit cells of the two-dimensional surface lattice in each plane are labeled respectively.

sputtering dose. The properties of the surface with different reconstructions are also examined.

This paper is organized as the following: after the description of sample preparation and characterization methods in Sec. II, Sec. III reports how the surface reconstruction and composition are tuned by  $\text{Ar}^+$  sputtering followed by UHV annealing, as well as by adsorption of Sr/Ti metals (also followed by UHV annealing). The later is more direct and easier to control, enabling us to establish the surface phase diagram in a wide range. In Sec. IV, we discuss that Ti diffuse towards the surface upon annealing and are responsible for the selective stabilization of different phases. Furthermore, we study the influence of different surface reconstructions on the electronic structures and metal adsorption behaviors. Finally the summary is presented in Sec. V.

## II. EXPERIMENTAL

The experiments were carried out in an Omicron variable temperature STM system equipped with LEED and XPS. The base pressure was better than  $1 \times 10^{-10}$  mbar. In XPS measurements, Mg  $K\alpha$  radiation and a pass energy of 20 eV were used. The binding energy was calibrated by using a copper metal ( $\text{Cu } 2p_{3/2}$  at 932.9 eV relative to the Fermi level). In another system equipped with low-temperature STM and reflective high-energy electron diffraction (RHEED), we carried out detailed and systematic imaging with high spatial resolution. All the STM images presented in this paper were along the same orientation as in Fig. 2 (a).

Nd-doped (0.7 wt%)  $\text{SrTiO}_3(110)$  single crystal ( $12 \text{ mm} \times 3 \text{ mm}$ ) were purchased from Hefei KMT Com-

pany, China. After loaded into the system, the as-received sample was sputtered with  $\text{Ar}^+$  beam at room temperature (RT) followed by annealing in UHV. The energy of the ion beam was varied from 0.5 to 2 KeV without any difference detected. The sample was heated by resistively passing a direct current through the crystal and the temperature was measured with an optical pyrometer. The annealing temperature was  $1000 \text{ }^\circ\text{C}$  for 1 hour unless otherwise specified. The pressure during annealing did not exceed  $2 \times 10^{-9}$  mbar. Ti metal was evaporated by using an electron beam evaporator while Sr metal was evaporated with a low temperature effusion cell. During the evaporation of Ti or Sr, the sample was at RT. The flux is 0.5 ML/min [ $1 \text{ ML} = 4.64 \times 10^{14}$  atoms/ $\text{cm}^2$  relative to  $\text{SrTiO}_3(110)$  surface] for both Sr and Ti, as calibrated by monitoring the RHEED intensity oscillation during the homoepitaxial growth of  $\text{SrTiO}_3(110)$  thin films. After metal evaporation, the sample was annealed with the same method as for the sputtered sample.

## III. RESULTS

### A. $\text{Ar}^+$ Sputtering

Figure 2 (a) shows two kinds of domains coexisting with each other on the surface of  $\text{SrTiO}_3(110)$  single crystal after  $\text{Ar}^+$  sputtering ( $0.5 \text{ KeV}/3.2 \mu\text{A}$  for 10 min) and UHV annealing. As shown in Fig. 2 (b), one type of the domains consists of periodic stripes along  $[1\bar{1}0]$  direction, separated by dark trenches, and each contains two obvious bright rows of periodic dots. The long-range ordering is characterized with the lattice constant of  $\sim 0.6 \text{ nm}$  along  $[1\bar{1}0]$  and  $1.6 \text{ nm}$  along  $[001]$ , respectively. Such a structure corresponds to the  $(4 \times 1)$ -reconstructed  $\text{SrTiO}$  termination, which has been observed by another group<sup>29,30</sup>. There are clusters adsorbed on the  $(4 \times 1)$  domain with uniform size of  $0.2 \text{ nm}$  in height and  $2 \text{ nm}$  in diameter. The distribution of the clusters also exhibits a quasi-long-range ordering – they form meandering lines along  $[001]$  and are separated by approximate “ $\times 10$ ” periodicity along  $[1\bar{1}0]$  as shown in Fig. 2 (d). The cluster density rises with Sr metal deposited at RT followed by annealing at  $300 \text{ }^\circ\text{C}$  for 0.5 h. The dependence of the increment of the cluster density on the Sr dosage is determined by the statistics of the STM images, indicating that there is only one Sr atom per cluster. The nature and the ordering mechanism of these  $\text{SrO}_x$  “magic” clusters are under further investigations.

As reported previously<sup>31</sup>, the height between  $(4 \times 1)$  and the other domain is about  $0.138 \text{ nm}$ , equivalent to the interspacing of adjacent  $(\text{SrTiO})^{4+}$  and  $(\text{O}_2)^{4-}$  atomic layers along  $[110]$  direction. The high-resolution STM image shows periodic protrusions along  $[1\bar{1}0]$  direction with the interspacing of  $\sim 0.3 \text{ nm}$ , as marked by dots in Fig. 2 (c). This is quite close to the value of  $\sqrt{2}/2a$  [ $a = 0.3905 \text{ nm}$ , the lattice constant of  $\text{SrTiO}_3(110)$  bulk

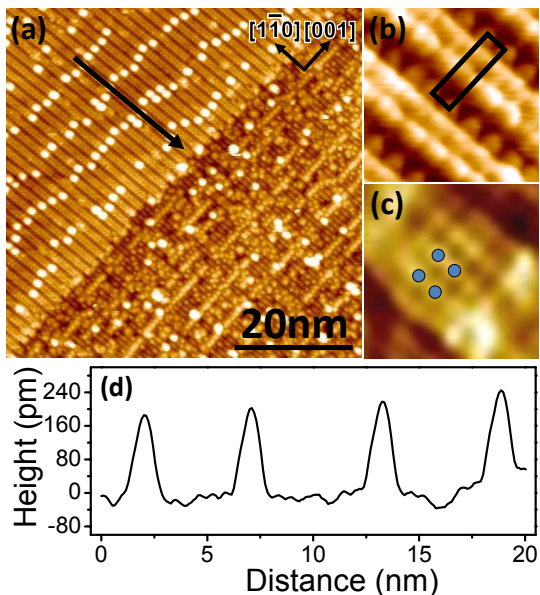


FIG. 2: (Color online) (a) STM image (1.5 V/20 pA) of SrTiO<sub>3</sub>(110) surface with SrTiO and O terminations coexisting with each other. (b) and (c) High resolution STM images of SrTiO (4×4 nm<sup>2</sup>, 1.0 V/200 pA) and O (2.6×2.6 nm<sup>2</sup>, 1.2 V/20 pA) terminations, respectively. The unit cell of the (4×1) reconstruction is labeled in the inset. (d) The line profile along the arrow in (a), indicating a ~“×10” periodicity of the clusters along [1 $\bar{1}$ 0].

crystal] that only possibly exists on the O-terminated surface [see Fig. 1 (b)], consistently indicating that the domain corresponds to the O termination. The detailed structure of the O-terminated surface will be discussed in the following.

We are able to tune the termination type on SrTiO<sub>3</sub>(110) by adjusting Ar<sup>+</sup> sputtering dose in each cleaning cycle. The surface with a single type of SrTiO or O termination can be obtained, respectively, as shown in Fig. 3 (a) and (c). With an intermediate sputtering dose, the two types of termination coexist with each other, as shown in Fig. 3 (b). We define the area ratio of SrTiO-terminated domains to the whole surface as  $S_{SrTiO}$ , which can be determined from the statistics over 8 STM images (500×500 nm<sup>2</sup>). On the other hand, the near surface atomic concentration is determined with the analyses of XPS spectra following:

$$[M] = \frac{I_M/\Sigma_M}{I_{Sr}/\Sigma_{Sr} + I_{Ti}/\Sigma_{Ti} + I_O/\Sigma_O}, \quad (1)$$

where M donates Sr, Ti or O, I is the integrated intensity of the characteristic peak in XPS for each element, and  $\Sigma$  is the element sensitivity factor that has been calibrated with vacuum fractured SrTiO<sub>3</sub>(001) surface<sup>32</sup>. As shown in Fig. 4, the near surface region composition changes with  $S_{SrTiO}$ . Terminated by SrTiO layer only ( $S_{SrTiO}=1$ ), the nominal composition of the near surface

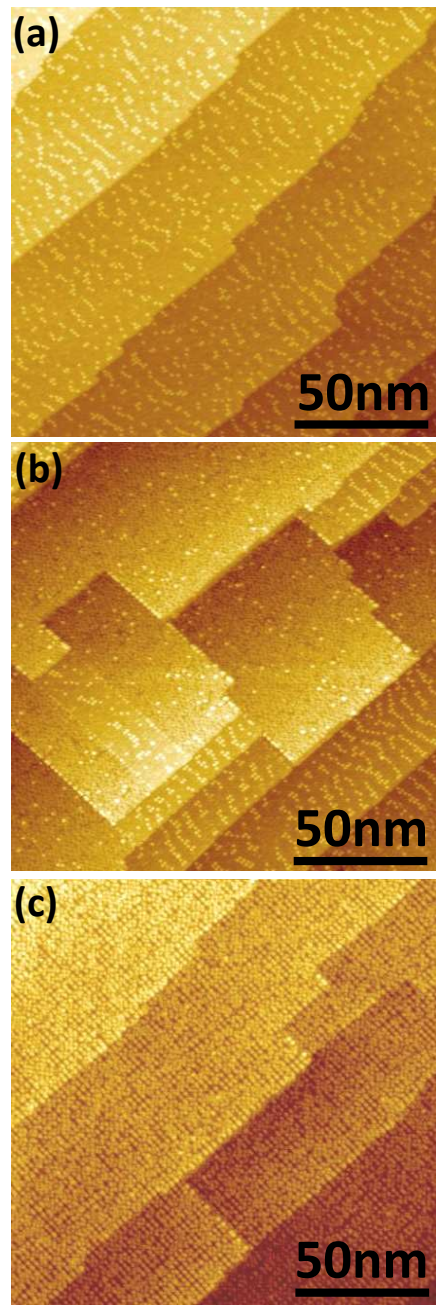


FIG. 3: (Color online) STM images (3.5 V/20 pA) of the SrTiO<sub>3</sub>(110) treated with different Ar<sup>+</sup> sputtering dose followed by annealing. As the sputtering dose increases, the surface evolves from (a) the single type of SrTiO termination to (b) the mixed SrTiO and O terminations, and to (c) the single type of O termination.

region is SrTi<sub>1.19</sub>O<sub>3.76</sub>, while it is SrTi<sub>1.5</sub>O<sub>4.5</sub> for the O-terminated sample ( $S_{SrTiO}=0$ ). The [Ti]/[Sr] increases from 1.19 to 1.5 monotonically as the surface evolves from SrTiO to O termination. It also should be noted that the (110) surface treated with Ar<sup>+</sup> sputtering followed by UHV annealing is not oxygen-deficient for either termination, at least not more deficient than the vacuum

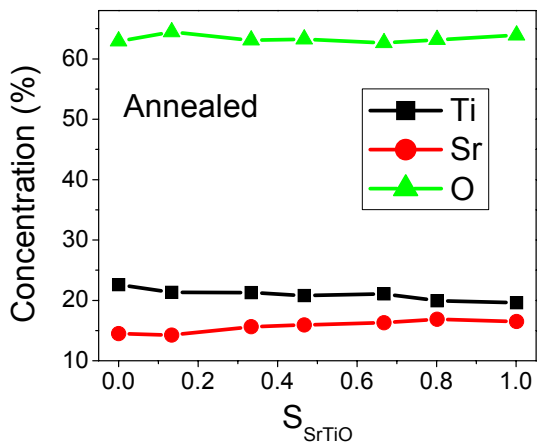


FIG. 4: (Color online) The near surface region chemical concentration of SrTiO<sub>3</sub>(110) (as determined by XPS) with different  $S_{SrTiO}$ .

fractured SrTiO<sub>3</sub>(001) surface that has been used for calibration.

### B. Adsorption of Sr and Ti metals

Treated with Ar<sup>+</sup> sputtering followed by annealing, the SrTiO<sub>3</sub>(110) surface is stable against high temperature or low oxygen partial pressure<sup>31</sup>. This suggests that thermodynamic equilibrium has been established on the surface and the stabilization process is strongly related to the chemical composition (Fig. 4). Therefore by directly evaporating Sr and/or Ti metals onto the surface, we can change the relative ratio of termination types. On the surface with SrTiO and O terminations coexisting [Fig. 5(a)], a submonolayer of Sr metal is evaporated. After annealing we obtain the surface with the single type of SrTiO termination [Fig. 5(b)]. Then by evaporating 0.08 ML Ti metal followed by annealing, O-terminated islands are formed [Fig. 5(c)]. As the dosage of Ti increasing, the area of O-terminated domains increases until the surface is fully covered by the single type of O termination.

Evaporating Sr or Ti metal followed by annealing induces the formation of SrTiO or O termination on the (110) surface, respectively. It is a reversible process in which  $S_{SrTiO}$  is determined by the dosage of Sr and Ti only, also characterized by the near surface [Ti]/[Sr] as determined by the XPS. Moreover, adjusting the evaporation dosage of Sr or Ti metal is practically easier and more precisely, which enables the detailed investigations of the evolution of different surface reconstructions beyond the simple identification of termination.

On SrTiO termination, we further increase the Sr concentration by evaporating  $\sim 0.05$  ML Sr onto the (4 $\times$ 1) monophased surface followed by annealing. New stripes are observed after annealing, as shown in Fig. 6(a). Each new stripe contains three bright rows of periodic dots

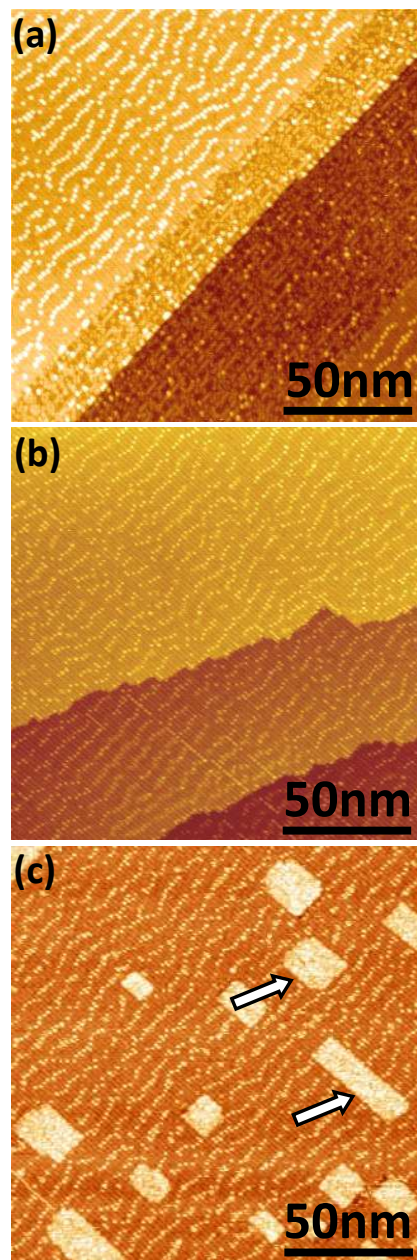


FIG. 5: (Color online) (a) STM image (2.0 V/20 pA) of (4 $\times$ 1)-reconstructed SrTiO termination coexisting with O termination. (b) (2.0 V/20 pA) The single type of SrTiO termination obtained by evaporating  $\sim 0.35$  ML Sr onto the surface in (a) followed by annealing. (c) (2.0 V/20 pA) The surface after depositing  $\sim 0.08$  ML Ti onto (b) followed by annealing. The arrows indicate O-terminated islands.

along [1 $\bar{1}$ 0] direction. There also exist hole-like defects on the center row, forming a quasi-ordering of “ $\times 10$ ” along [1 $\bar{1}$ 0]. The domain area of new stripes enlarges with Sr evaporation dosage increasing until a monophased surface formed with  $\sim 0.15$  ML Sr, as shown in Fig. 6(b). The high-resolution STM image shows the new long-range ordering with a lattice constant of  $\sim 0.6$  nm along

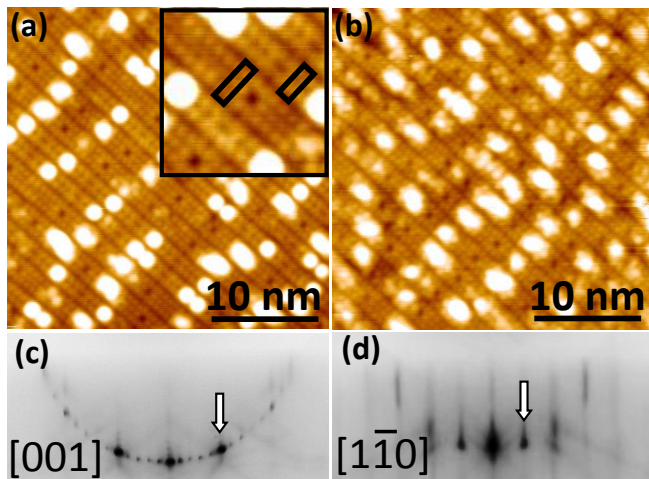


FIG. 6: (Color online) (a) (1.6 V/20 pA) The surface with  $(5 \times 1)$  and  $(4 \times 1)$  phases coexisting with each other. The unit cells are labeled in the inset with rectangles, respectively. (b) (1.5 V/20 pA) The monophased  $(5 \times 1)$  surface. (c) and (d) The RHEED patterns of  $(5 \times 1)$  along  $[001]$  and  $[1\bar{1}0]$  directions, respectively. The integral diffractions are indicated by arrows.

$[1\bar{1}0]$  and  $\sim 1.95$  nm along  $[001]$ , respectively, consistent with the RHEED patterns that clearly indicate the  $(5 \times 1)$  reconstruction. There are clusters adsorbed on the  $(5 \times 1)$  surface. Their size and distribution are random and do not relate to the annealing temperature or the cleanliness of the chamber.

Evaporating Ti metal onto the surface enlarges the  $(4 \times 1)$  domain over  $(5 \times 1)$ . The reversed phase transition from  $(5 \times 1)$  to  $(4 \times 1)$  reconstruction can be realized by evaporating  $\sim 0.15$  ML Ti followed by annealing.

As discussed above, Ti induces the formation of O-termination on the surface. By evaporating  $\sim 0.75$  ML Ti onto the  $(4 \times 1)$  monophased surface, we change it into the single type of O termination after annealing. Bright rows along  $[1\bar{1}0]$  are observed in the high-resolution STM image in Fig. 7 (a). The line profile across the rows indicates a periodicity of  $\sim 0.75$  nm along  $[001]$ . Protrusions in the rows are marked by the dots with the interspacing of  $\sim 0.3$  nm, suggesting that they slightly pair up along  $[001]$ . As indicated by the white dashed lines, dark trenches present with an interspacing of  $\sim 2.3$  nm along  $[1\bar{1}0]$ , forming the “ $\times 8$ ” periodicity relative to the lattice periodicity in O atomic layer ( $\sqrt{2}/2a$ ). Such a  $(2 \times 8)$  reconstruction is clearly visible in the RHEED patterns shown in Fig. 7 (c) and (d). Note that the integral diffractions in the RHEED patterns correspond to different surface lattice constant along  $[1\bar{1}0]$  as compared to that of SrTiO termination, since RHEED sensitively reflects their different irreducible surface unit cells (see Fig. 1). The surface is densely adsorbed by clusters that can be divided into two categories by size. The small clusters are on top of the paired rows with random distribution. The big clusters are over the trenches between

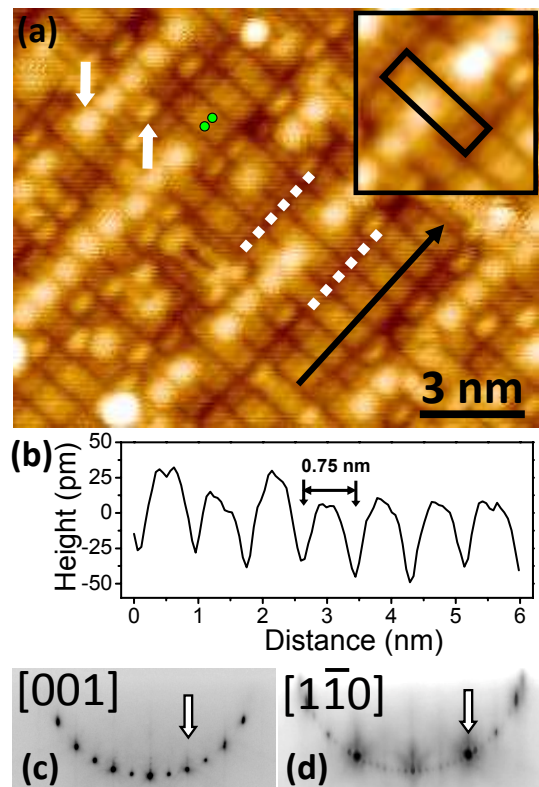


FIG. 7: (Color online) High-resolution STM image (1.5 V/40 pA) of the monophased  $(2 \times 8)$  surface. As labeled with (green) dots, the protrusions in the image pair up along  $[001]$ . The dark trenches along  $[001]$  are labeled with white dashed lines, while two kinds of clusters are indicated by the bright up and down arrows, respectively. The  $(2 \times 8)$  unit cell is labeled in the zoom-in image in the inset. (b) The line profile along the black line in (a). (c) and (d) The  $(2 \times 8)$  RHEED patterns along  $[001]$  and  $[1\bar{1}0]$  directions, respectively, with the integral diffractions indicated with arrows.

the paired rows, and align to straight lines along  $[001]$ . These clusters seem to be intrinsic for the  $(2 \times 8)$  phase and might be responsible for the charge compensation on the O-terminated SrTiO<sub>3</sub>(110) polar surface, although the detailed mechanism is not understood yet.

Further increasing the Ti dosage on the  $(2 \times 8)$  surface followed by annealing, a structural phase transition to  $(6 \times 8)$  occurs with the dosage of  $\sim 0.1$  ML. Comparing to the uniform row pairs in the  $(2 \times 8)$  phase, wide stripes with four protrusions in across appear, which are arranged alternatively with the row pairs, as shown in Fig. 8 (a). The  $(6 \times 8)$  long-range ordering is clearly shown by the RHEED patterns. There are two different kinds of clusters adsorbed on the surface. One is the bean-like cluster adsorbed on top of the “ $4 \times$ ” stripe, arranged in a perfect  $(6 \times 8)$  order. The other is the round cluster adsorbed between the “ $4 \times$ ” and “ $2 \times$ ” stripes with a lower density. It should be noted that in the high-resolution STM image, there are only 7 protrusions in one “ $\times 8$ ” unit cell along  $[1\bar{1}0]$  either on the  $2 \times$  or  $4 \times$  stripes.

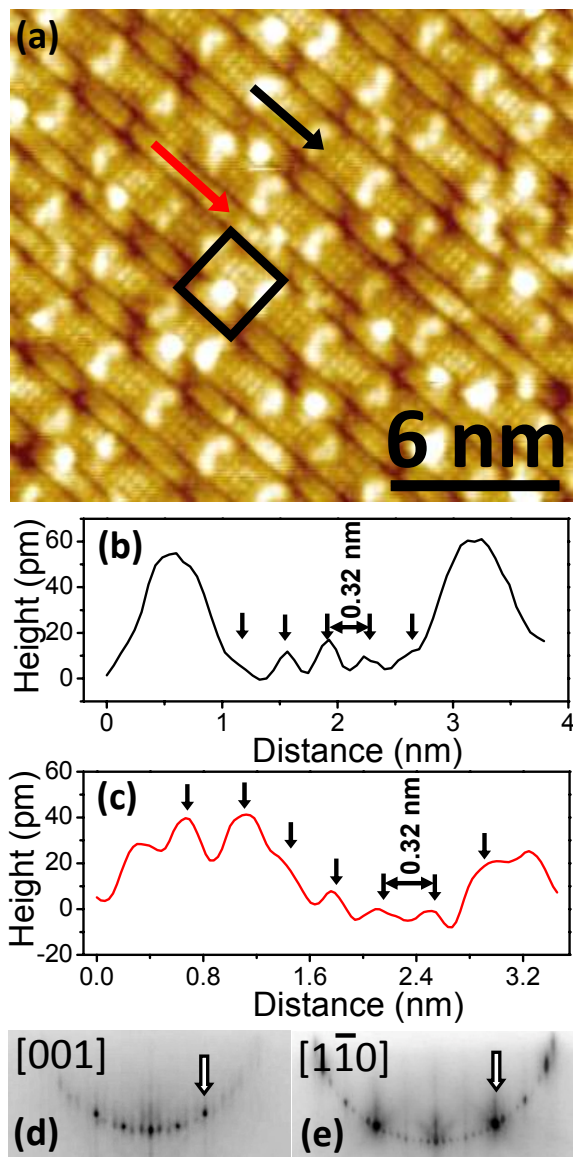


FIG. 8: (Color online) STM image (1.0 V/20 pA) of the monophased ( $6\times 8$ ) surface. The unit cell is labeled with the rectangle. (b) and (c) Line profiles along the black and red (grey) arrows in (a), respectively. (d) and (e) The ( $6\times 8$ ) RHEED patterns along  $[001]$  and  $[1\bar{1}0]$  directions, respectively, with the integral diffractions indicated with arrows.

The interspacing between two protrusions is  $\sim 0.32$  nm, showing the  $8/7$  “magic” lattice match to the bulk truncated O atomic layer.

Figure 9 shows the surface after evaporating  $\sim 0.05$  ML Sr onto the monophased ( $6\times 8$ ) followed by annealing. Some “ $2\times$ ” stripes condensate together forming ( $2\times 8$ ) domains. The reversible structural phase transition between ( $2\times 8$ ) and ( $6\times 8$ ) can be realized by evaporating  $\sim 0.1$  ML Ti or Sr metal.

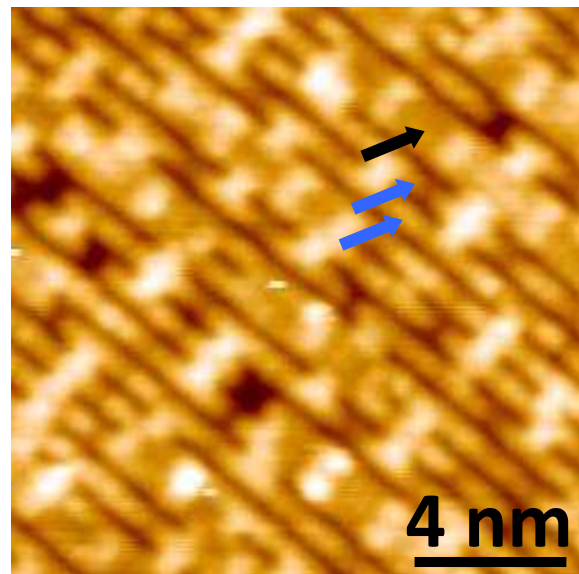


FIG. 9: (Color online) STM image (1.5 V/20 pA) of the surface after evaporating  $\sim 0.05$  ML Sr onto the monophased ( $6\times 8$ ) followed by annealing. The “ $4\times$ ” and “ $2\times$ ” stripes are indicated with black and blue (grey) arrows, respectively.

#### IV. DISCUSSION

We establish a clear surface phase diagram in a broad range of chemical concentrations. As the evaporation dosage of Ti increases, the surface transforms from the ( $5\times 1$ )-reconstructed SrTiO termination to ( $4\times 1$ ), then to ( $2\times 8$ )-reconstructed O termination, and finally to ( $6\times 8$ ). Reversible phase transitions can be induced by increasing Sr evaporation dosage. All the surface reconstructions are stable at high temperatures up to  $1100$  °C and under oxygen partial pressure from UHV to  $1\times 10^{-4}$  mbar. On the surface with mixed phases, the relative area ratio of different domains keeps constant within the ranges of temperature and oxygen partial pressure as above, without any other phase developing. It is concluded that thermodynamic equilibrium has been reached on the surface and the stabilization of the reconstruction phases is determined by  $[\text{Ti}]/[\text{Sr}]$ .

The surface composition can also be varied reversibly by  $\text{Ar}^+$  sputtering with different dose followed by annealing, resulting in different area ratio of SrTiO and O terminations, *i.e.*,  $S_{\text{SrTiO}}$  (see Fig. 3 and 4). This is also a thermodynamic process determined by  $[\text{Ti}]/[\text{Sr}]$  in the near surface region. As shown in Fig. 10, both  $S_{\text{SrTiO}}$  and  $[\text{Ti}]/[\text{Sr}]$  on the annealed surface get saturated quickly after a few repeated treatment cycles with fixed parameters, unrelated to the initial configuration on the surface. Detailed high-resolution STM investigations actually reveal the reversible phase transitions between all the reconstructions can be realized by elaborately tuning the sputtering dose.

However, with XPS analyses, we found that the

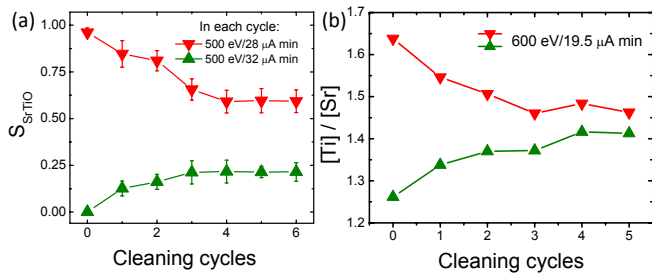


FIG. 10: (Color online) (a) and (b)  $S_{SrTiO}$  and  $[Ti]/[Sr]$  of the sample with different number of repeated cycles of cleaning (500 eV-sputtering followed by annealing), respectively. The statistics of  $S_{SrTiO}$  are done over 8 STM images ( $500 \times 500 \text{ nm}^2$ ) for each data point. The sputtering dose is fixed for each series of cleaning cycles.

$[Ti]/[Sr]$  is equal to 1 for the as-sputtered samples, and almost keeps constant for different sputtering dose, as shown in Fig. 11. No preferential sputtering by  $Ar^+$  has been observed within the ion energy range of 0.5 to 2 keV, which is different from the results on  $SrTiO_3(001)$  and (111) surfaces<sup>17,33</sup>. However,  $[Ti]/[Sr]$  increases dramatically after annealing in relative to the as-sputtered sample, and the increment becomes larger monotonically as the sputtering dose increasing, as plotted in Fig. 11 (b). It is suggested that Ti (or Ti-O species) tend to diffuse towards the surface upon annealing to establish the thermodynamic equilibrium. Similarly, Ti-enriched nanostructures or even anatase  $TiO_2$  islands have been obtained on the  $SrTiO_3(001)$  surfaces by intensive  $Ar^+$  sputtering followed by annealing<sup>14–17</sup>.

The high-resolution XPS presented in Fig. 12 confirm the picture. On the annealed sample, well-defined Ti  $2p$  and Sr  $3d$  core-level spectra are observed. The Ti  $2p$  spectrum shows the single spin-orbital doublet feature of  $Ti^{4+}$  state as in the bulk crystal of  $SrTiO_3$ . The Sr  $3d$  spectrum can be fitted with two spin-orbital doublet pairs that originate from different chemical coordination of Sr. The main doublet feature centered at  $\sim 133$  eV is the characteristic of perovskite crystal, while the other fea-

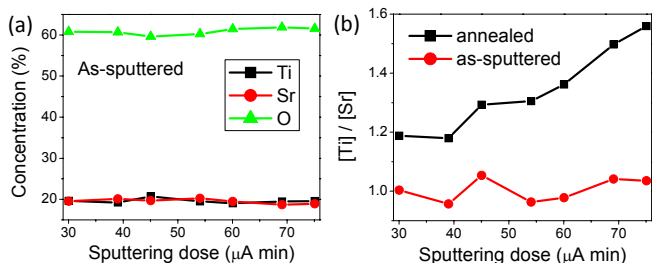


FIG. 11: (Color online) (a) The surface chemical concentration of the as-sputtered  $SrTiO_3(110)$  surface determined by XPS. (b)  $[Ti]/[Sr]$  of the as-sputtered and annealed surface, respectively. Each data point in (a) and (b) is the saturated value after several repeated cycles of treatment with the fixed sputtering dose, respectively.

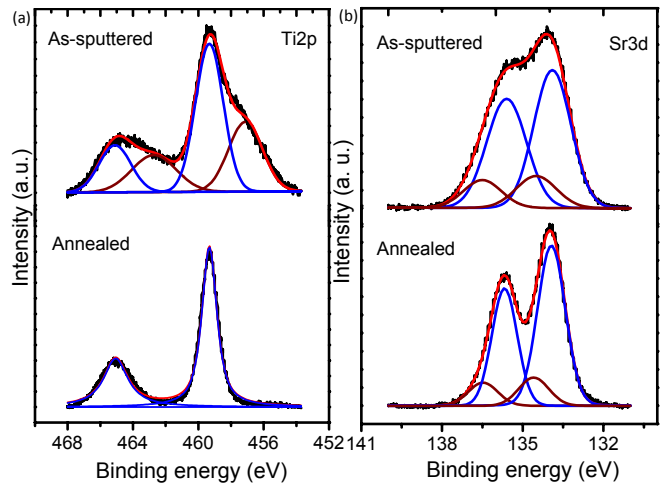


FIG. 12: (Color online) (a) Ti  $2p$  core-level spectra of the annealed (lower panel) and as-sputtered (upper panel) surfaces, respectively. The spectrum taken on the annealed surface is fitted with a single doublet feature, while the as-sputtered surface spectrum is fitted with an additional doublet feature shifted to lower binding energy by  $\sim 1.65$  eV. (b) The Sr  $3d$  core-level spectra of the annealed (lower panel) and as-sputtered (upper panel) surfaces, respectively.

ture shifting towards higher energy by  $\sim 0.9$  eV can be attributed to Sr-O bond on the surface<sup>34–36</sup>. In contrast, on the as-sputtered sample, the two peaks corresponding to Ti  $2p$  single doublet state show broad shoulders at  $\sim 456.7$  eV and 462.5 eV, respectively, indicating the appearance of  $Ti^{3+}$ <sup>37</sup>. This is consistent with recent first-principles calculations that have revealed the existence of Ti antilike defects<sup>38</sup>. In Sr  $3d$  spectrum, the weight of high-energy doublet feature is higher than that on the annealed surface, consistently showing that the as-sputtered surface is deeply separated into SrO and  $TiO_x$  chemical coordinations.

Considering the fact that titanium oxide have lower surface free energy as compared to the  $SrTiO_3$ <sup>14,15,30</sup>, those under-coordinated Ti induced by sputtering is

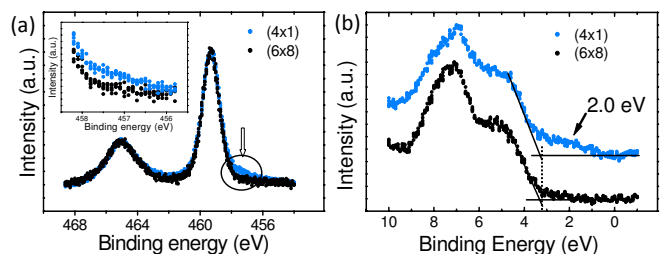


FIG. 13: (Color online) (a) Ti  $2p$  core-level spectra taken on the monophased (4 $\times$ 1) and (6 $\times$ 8) surfaces, respectively. The inset zooms in their difference showing the appearance of  $Ti^{3+}$  component on the (6 $\times$ 8) surface. (b) The valence-band spectra of the two reconstructions, respectively. The in-gap states are labeled with arrow.

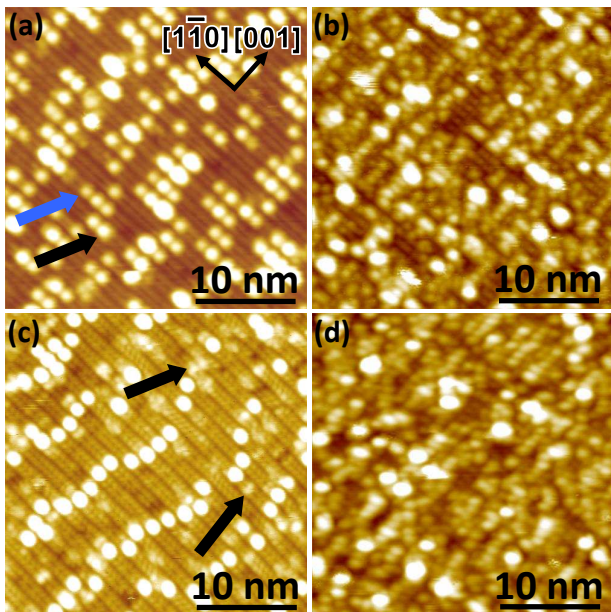


FIG. 14: (Color online) (a) and (b) STM images (1.0 V/20 pA) of the (4×1) and (2×8) surfaces evaporated with 0.02 ML Sr at RT, respectively. The original clusters and the evaporated Sr are indicated with black and blue (grey) arrows, respectively. (c) and (d) STM images (1.5 V/20 pA) of the (4×1) and (2×8) surfaces evaporated with 0.02 ML Ti at RT, respectively. The as-deposited Ti are indicated with black arrows.

driven to diffuse towards the surface upon annealing. Therefore the established thermodynamic equilibrium can be described as a Ti-enriched surface covering the stoichiometric SrTiO<sub>3</sub> bulk crystal. As the sputtering dose increases, the depth of the affected region increases and consequently the overall amount of Ti defects available to diffuse increases. After annealing, all the diffusive Ti accumulate within a few surface layers and the concentration increment will be fully manifested by XPS. Such a mechanism determines the intrinsic dependence of the near surface chemical composition of SrTiO<sub>3</sub>(110) on the sputtering dose, offering the tunability of different reconstructions by adjusting the sputtering dose that is equivalent to evaporating Sr or Ti metal.

To further examine the properties of SrTiO<sub>3</sub>(110) surface with different reconstructions, XPS core-level and valence-band spectra are carefully compared. Figure 13 (a) shows Ti 2*p* core-level spectra taken from the monophased (4×1) and (6×8) surface, respectively. The (4×1) surface shows mainly the Ti<sup>4+</sup> characteristic, while the (6×8) surface also shows the existence of Ti<sup>3+</sup> species as revealed by the low-energy shoulder<sup>39–41</sup>. This is consistent with the chemical composition analyses that indicates the Ti enrichment on O termination. Figure 13 (b) compares the valence-band spectra of the (4×1)- and (6×8)-reconstructed surfaces. The highest occupied state is determined by linearly extrapolating the onset of spectra. The corresponding binding energy

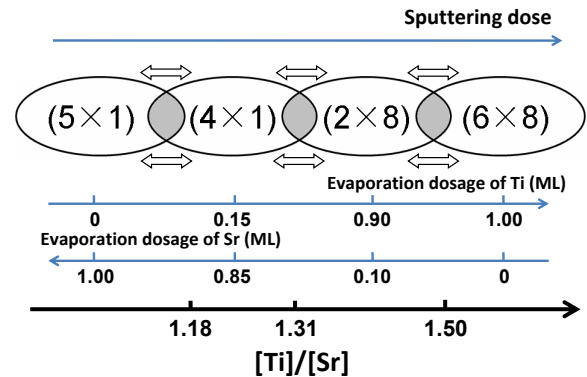


FIG. 15: (Color online) The phase diagram of SrTiO<sub>3</sub>(110) surface in relative to [Ti]/[Sr] that can be tuned by the sputtering or evaporating Sr or Ti metal.

in relative to Fermi energy ( $E_F$ ) is  $E_F - E_{VB} = 3.3$  eV. As the bandgap of the SrTiO<sub>3</sub> is  $E_g = 3.3$  eV<sup>42</sup>, this value indicates that the  $E_F$  is near the minimum of the conduction band. In-gap states arise at  $\sim 2.0$  eV below  $E_F$  on the (6×8) surface, indicating the existence of Ti<sup>3+</sup> species<sup>41,43</sup>, which is consistent with the Ti 2*p* core-level spectra. The appearance of the in-gap states also suggests that the O-terminated SrTiO<sub>3</sub>(110) polar surface can be stabilized by filling electrons to extra states, in addition to the stoichiometry modification and adsorption of (charged) clusters.

Since the surface electronic structure is varied with different reconstructions, the initial epitaxial growth behavior is also influenced. Figure 14 shows the different adsorption behaviors of Sr and Ti metals on the (4×1)- and (2×8)-reconstructed surfaces. With  $\sim 0.02$  ML Sr adsorbed onto (4×1) at RT, there are round protrusions appearing in the STM image, darker and smaller than those original clusters, as shown in Fig. 14 (a). By the statistics of the density of the adsorbed clusters, we found that Sr adsorb on (4×1) as isolated single adatoms on top of the “4×” stripes. Increasing the Sr dosage results in a higher density of the adatoms whose distribution still strictly follows the stripes. Sr atoms adsorbed on the (2×8) phase aggregate into randomly distributed clusters with nonuniform size. This might be the result of the strong interaction of Sr atoms with the (2×8)-reconstructed surface due to its high reactivity. The adsorption behavior of Ti atoms is different from that of Sr adatoms. They aggregate into randomly distributed clusters with nonuniform size on the both (4×1) and (2×8) reconstructions.

## V. SUMMARY

We establish a clear phase diagram of SrTiO<sub>3</sub>(110) surface, as shown in Fig. 15. The surface can be selected from the (5×1)- to (4×1)-reconstructed SrTiO termination, then to (2×8)- and finally to (6×8)-reconstructed O termination. All the structural phase transitions are

reversibly driven by the change of the  $[\text{Ti}]/[\text{Sr}]$ , which can be tuned by adjusting the sputtering dose or the amount of Sr/Ti adsorption. These two tuning methods are equivalent because the under-coordinated Ti induced by sputtering tend to diffuse towards the surface upon annealing. The electronic states of pure  $\text{Ti}^{4+}$  valence are detected on  $(4\times 1)$ . In contrast, they are mixed with  $\text{Ti}^{3+}$  on  $(6\times 8)$ . This leads the O termination more active than the SrTiO termination, resulting in different absorption behaviors during the initial epitaxial growth.

### **Acknowledgments**

This work is supported by Chinese NSF-10704084 and Chinese MOST (2006CB921300 & 2007CB936800).

- 
- \* Electronic address: [jdguo@aphy.iphy.ac.cn](mailto:jdguo@aphy.iphy.ac.cn)
- <sup>1</sup> J. Heber, *Nature* **459**, 28 (2009).
  - <sup>2</sup> A. Ohtoma and H. Y. Hwang, *Nature* **427**, 423 (2004).
  - <sup>3</sup> D. F. Bogorin, P. Irvin, C. Cen, and J. Levy, arXiv:1011.5290.
  - <sup>4</sup> C. H. Ahn, K. M. Rabe, and J. M. Triscone, *Science* **303**, 488 (2004).
  - <sup>5</sup> H. N. Lee, H. M. Christen, M. F. Chisholm, C. M. Rouleau, and D. H. Lowndes, *Nature (London)* **433**, 395 (2005).
  - <sup>6</sup> D. G. Schlom, J. H. Haeni, J. Lettieri, C. D. Theis, W. Tian, J. C. Jiang, and X. Q. Pan, *Mater. Sci. Eng. B* **87**, 282 (2001).
  - <sup>7</sup> I. Bozovic, *IEEE Trans. Appl. Supercond.* **11**, 2686 (2001).
  - <sup>8</sup> S. J. May, P. J. Ryan, J. L. Robertson, J.-W. Kim, T. S. Santos, E. Karapetrova, J. L. Zarestky, X. Zhai, S. G. E. te Velthuis, J. N. Eckstein, S. D. Bader, and A. Bhattacharya, *Nature Mater.* **8**, 892 (2009)
  - <sup>9</sup> N. Takubo, Y. Ogimoto, M. Nakamura, H. Tamaru, M. Izumi, and K. Miyano, *Phys. Rev. Lett.* **95**, 017404 (2005).
  - <sup>10</sup> M. Kawasaki, K. Takahashi, T. Maeda, R. Tsuchiya, M. Shinohara, O. Ishiyama, T. Yonezawa, M. Yoshimoto, and H. Koinuma, *Science* **266**, 1540 (1994).
  - <sup>11</sup> G. Koster, B. L. Kropman, G. J. H. M. Rijnders, D. H. A. Blank, and H. Rogalla, *Appl. Phys. Lett.* **73**, 2920 (1998).
  - <sup>12</sup> T. Kubo and H. Nozoye, *Phys. Rev. Lett.* **86**, 1801 (2001).
  - <sup>13</sup> T. Kubo and H. Nozoye, *Surf. Sci.* **542**, 177 (2003).
  - <sup>14</sup> N. Erdman, K. R. Poeppelmeier, M. Asta, O. Warschkow, D. E. Ellis, and L. D. Marks, *Nature* **419**, 55 (2002).
  - <sup>15</sup> N. Erdman, O. Warschkow, M. Asta, K. R. Poeppelmeier, D. E. Ellis, and L. D. Marks, *J. Am. Chem. Soc.* **125**, 10050 (2003).
  - <sup>16</sup> B. C. Russell and M. R. Castell, *Phys. Rev. B* **75**, 155433 (2007).
  - <sup>17</sup> B. C. Russell and M. R. Castell, *J. Phys. Chem. C* **112**, 6538 (2008).
  - <sup>18</sup> R. Herger, P. R. Willmott, O. Bunk, C. M. Schleptuz, B. D. Patterson, and B. Delley, *Phys. Rev. Lett.* **98**, 076102 (2007).
  - <sup>19</sup> Q. D. Jiang and J. Zegenhagen, *Surf. Sci.* **425**, 343 (1999).
  - <sup>20</sup> M. R. Castell, *Surf. Sci.* **516**, 33 (2002).
  - <sup>21</sup> F. Silly, D. T. Newell, and M. R. Castell, *Surf. Sci.* **600**, L219 (2006).
  - <sup>22</sup> D. T. Newell, A. Harrison, F. Silly, and M. R. Castell, *Phys. Rev. B* **75**, 205429 (2007).
  - <sup>23</sup> C. Noguera, *J. Phys.: Condens. Matter* **12**, R367 (2000).
  - <sup>24</sup> J. Goniakowski, F. Finocchi, and C. Noguera, *Rep. Prog. Phys.* **71**, 016501 (2008).
  - <sup>25</sup> M. Takizawa, Y. Hotta, T. Susaki, Y. Ishida, H. Wadati, Y. Takata, K. Horiba, M. Matsunami, S. Shin, M. Yabashi, K. Tamasaku, Y. Nishino, T. Ishikawa, A. Fujimori, and H. Y. Hwang, *Phys. Rev. Lett.* **102**, 236401 (2009).
  - <sup>26</sup> F. Bottin, F. Finocchi, and C. Noguera, *Phys. Rev. B* **68**, 035418 (2003).
  - <sup>27</sup> J. Brunen and J. Zegenhagen, *Surf. Sci.* **389**, 349 (1997).
  - <sup>28</sup> H. Bando, Y. Aiura, Y. Haruyama, T. Shimizu, and Y. Nishihara, *J. Vac. Sci. Technol. B* **13**, 1150 (1995).
  - <sup>29</sup> B. C. Russell and M. R. Castell, *Phys. Rev. B* **77**, 245414 (2008).
  - <sup>30</sup> J. A. Enterkin, A. K. Subramanian, B. C. Russell, M. R. Castell, K. R. Poeppelmeier, and L. D. Marks, *Nature Mater.* **9**, 245 (2010).
  - <sup>31</sup> Z. Wang, K. Wu, Q. Guo, and J. Guo, *Appl. Phys. Lett.* **95**, 021912 (2009).
  - <sup>32</sup> The sensitivity factors are  $\Sigma_{Sr}=1.843$ ,  $\Sigma_{Ti}=2.001$ , and  $\Sigma_O=0.711$ , respectively.
  - <sup>33</sup> W. J. Lo and G. A. Somorjai, *Phys. Rev. B* **17**, 4942 (1978).
  - <sup>34</sup> K. Szot, W. Speier, U. Breuer, R. Meyer, J. Szade, and R. Waser, *Surf. Sci.* **460**, 112 (2000).
  - <sup>35</sup> W. D. Yang, *J. Mater. Sci.* **34**, 3533 (1999).
  - <sup>36</sup> R. Courths, J. Noffke, H. Wern, and R. Heise, *Phys. Rev. B* **42**, 9127 (1990).
  - <sup>37</sup> C. Webb, M. Lichtensteiger, *Surf. Sci.* **107**, L345 (1981).
  - <sup>38</sup> M. Choi, F. Oba, and I. Tanaka, *Phys. Rev. Lett* **103**, 185502 (2009).
  - <sup>39</sup> M. Copel, P. R. Duncombe, D. A. Neumayer, T. M. Shaw, and R. M. Tromp, *Appl. Phys. Lett.* **70**, 3227 (1997).
  - <sup>40</sup> M. Dawber, J. F. Scott, and A. J. Hartmann, *J. Eur. Ceram. Soc.* **21**, 1633 (2001).
  - <sup>41</sup> V. E. Henrich, G. Dresselhaus, and H. J. Zeiger, *Phys. Rev. B* **17**, 4908 (1978).
  - <sup>42</sup> M. Cardona, *Phys. Rev.* **140**, A651 (1965).
  - <sup>43</sup> M. Nolan, S. D. Elliott, J. S. Mulley, R. A. Bennett, M. Basham, and P. Mulheran, *Phys. Rev. B* **77**, 235424 (2008).